https://doi.org/10.1016/j.matdes.2018.04.012 **This is the Pre-Published Version.**
Ms. Ref. No.: JMAD-D-17-07605 (AFM17-0308063-S2:SSND-P)

Thickness-dependent structural and electromechanical properties of $(Na_{0.85}K_{0.15})_{0.5}Bi_{0.5}TiO_3$ multilayer thin film-based heterostructures

Yunyi Wu [a,b,c], Siu Wing Or [a,b,*]

[a] *Department of Electrical Engineering, The Hong Kong Polytechnic University, Hung Hom, Kowloon, Hong Kong*

[b] *Hong Kong Branch of National Rail Transit Electrification and Automation Engineering Technology Research Center, Hong Kong*

[c] *Department of Energy Materials and Technology, General Research Institute for Nonferrous Metals, Beijing, China*

** Corresponding author. E-mail address: eeswor@polyu.edu.hk (S. W. Or).*

ABSTRACT

$(Na_{0.85}K_{0.15})_{0.5}Bi_{0.5}TiO_3$ (NKBT) multilayer thin films with different thicknesses of 100–700 nm, corresponding to 2–14 layers with each layer of ~50 nm thickness, are synthesized on Pt(111)/Ti/SiO_2/Si substrates to form Pt/NKBT/Pt/Ti/SiO_2/Si heterostructures using different spin-coating and annealing conditions in a modified aqueous sol-gel process. The multilayer thin films spin-coated by two steps (step 1/2) at 600/4000 rpm for 6/30 s and annealed at 700 °C for 5 min with a heating rate of 30 °C/s show a dense, uniform, and continuous morphology as well as a pure perovskite structure with a rhombohedral–tetragonal phase transition at ~140 °C and no preferential orientation in the heterostructures. Their structural and electromechanical properties exhibit consistent improvement trends with increasing thickness from 100 to 550 nm (i.e., 2–11 layers). The 550 nm-thick, 11-layer films demonstrate the best ferroelectric, dielectric, piezoelectric, and electric performance in terms of the highest remnant polarization, saturation polarization, dielectric constant, and effective piezoelectric constant of 18.3 μC/cm^2, 53.6 μC/cm^2, 463, and 64 pm/V, as well as the lowest coercive field, dielectric loss tangent, and leakage current density of 116 kV/cm, 0.057, and 27 μA/cm^2, respectively. The observed thickness-dependent improvement is explained by an interfacial passive layer effect where the motion of both 180º and non-180º domain walls is enhanced in the thicker multilayer thin films by weakening the influence of domain pinning in the interfacial passive layers between the multilayer thin films and the substrates.

GRAPHICAL ABSTRACT

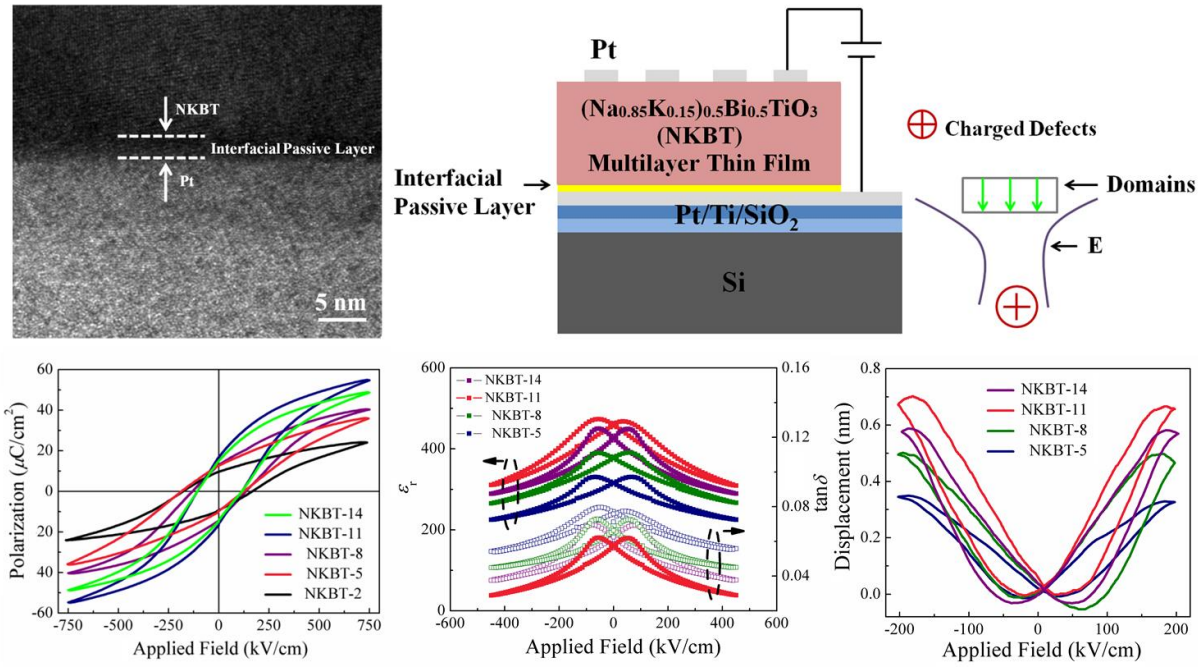

HIGHLIGHTS

- $(Na_{0.85}K_{0.15})_{0.5}Bi_{0.5}TiO_3$ multilayer thin films of different thicknesses were synthesized on Pt(111)/Ti/SiO_2/Si substrates.
- An optimal set of process conditions was obtained by studying different spin-coating and annealing heating rate conditions.
- The structural and electromechanical properties exhibit consistent improvement trends with increasing thickness to ~550 nm.
- An interfacial passive layer was observed and its effect on the thickness-dependent property improvement was explained.

Keywords:

Heterostructures; Interfacial passive layer; Lead-free piezoelectric; Multilayer thin films; Thickness-dependent properties

1. Introduction

Sodium bismuth titanate, $Na_{0.5}Bi_{0.5}TiO_3$ (NBT), perovskite ceramic is regarded as a fundamental lead-free ferroelectric ceramic because of its strong ferroelectricity with large remnant polarization (P_r) of 38 $\mu C/cm^2$ and high Curie temperature (T_C) of 320 °C [1,2]. Potassium bismuth titanate, $K_{0.5}Bi_{0.5}TiO_3$ (KBT), modified NBT, namely sodium–potassium bismuth titanate (NKBT or NBT–KBT) and with the chemical formula of $(Na_{1-x}K_x)_{0.5}Bi_{0.5}TiO_3$ or $(1–x)(Na_{0.5}Bi_{0.5})TiO_3–x(K_{0.5}Bi_{0.5})TiO_3$, has been evolved as a key lead-free piezoelectric ceramic system over the past decade by reducing the difficulty in poling caused by the high electrical conductivity, large leakage current density, and high coercive field in the unmodified NBT [3–5]. The NKBT ceramic system has been found to exhibit obviously improved electromechanical properties at the rhombohedral–tetragonal morphotropic phase boundary (MPB) with the composition of $x = 0.15$, giving rise to $(Na_{0.85}K_{0.15})_{0.5}Bi_{0.5}TiO_3$ or $0.85(Na_{0.5}Bi_{0.5})TiO_3–0.15(K_{0.5}Bi_{0.5})TiO_3$ ceramic [3–5]. The research on NKBT has also attracted much attention to synthesize high-quality thin films using various methods and processes in addition to the investigation of the relationships with their compositions, microstructures, and electromechanical properties [6–10].

With the rapid development of sensing, actuation, transduction, and energy devices towards miniaturization and multifunction in recent years, the abilities to synthesize high-quality lead-free piezoelectric thin films and to integrate them with micro-/nano-electronics to form micro-/nano-systems with high compatibility and performance are becoming increasingly important and concerned [11]. In fact, an increase in miniaturization and multifunction of micro-/nano-systems requires the corresponding scaling down of the dimensions of the piezoelectric thin films. Among all dimensions, thickness plays a determinative role in thin-film integration [11]. Since piezoelectricity is a cooperative phenomenon of the thin films and their substrates, it is both scientifically and technologically imperative to understand the effects of thin-film thickness on the physical properties of the resulting thin film–substrate heterostructures, especially when the thin films are to be synthesized on those substrates having specific configurations and/or properties [12–15].

Recently, thin nonferroelectric passive layers with low dielectric constants have been observed at the interface between ferroelectric thin films and their substrates, such as in the $Pt/SrTiO_3/Pt/MgO$ and $Pt/BaTiO_3/LSCO/MgO$ heterostructures, as a result of some

interfacial reaction during synthesis processes [14,15]. These interfacial passive layers behave electrically as parasitic interfacial capacitors in series with the interior of the ferroelectric thin films to suppress dielectric constants. Some studies have ever pointed out that the interfacial strains induced by lattice distortion in the interfacial passive layers act as potential wells to trap charged defects (e.g., oxygen vacancies), thereby creating domain-pinning centers to constrain the domain-wall motion in the ferroelectric thin films near the interface [16,17]. While crucial for scientific research and technological application of the NKBT thin films, there does not appear to be any major work disclosing their thickness-dependent physical properties and interfacial passive layer effect, especially in NKBT multilayer thin film-based heterostructures.

In this paper, we synthesize NKBT multilayer thin films with the composition of $(Na_{0.85}K_{0.15})_{0.5}Bi_{0.5}TiO_3$ at different layer numbers of 2–14 on Pt(111)/Ti/SiO_2/Si substrates to form Pt/NKBT/Pt/Ti/SiO_2/Si heterostructures of different NKBT multilayer thin film thicknesses of 100–700 nm using different conditions of spin coating and annealing heating rate in a modified aqueous sol-gel process in order to study the synthesis process and optimize the process conditions. We then investigate the thickness dependence on structural and electromechanical (i.e., ferroelectric, dielectric, piezoelectric, and electric) properties of the NKBT multilayer thin films in the Pt/NKBT/Pt/Ti/SiO_2/Si heterostructures so as to reveal the underlying interfacial passive layer effect and provide a thickness-dependent interfacial passive layer model for the NKBT multilayer thin film-based heterostructures. It is noted that a modified aqueous sol-gel process, which is more environmentally friendly and integratable with semiconductor technologies, is used to avoid hydrolyzation of metal alkoxide, formation of precipitation, and reflux of organic solvents (e.g., ethylene glycol monomethyl ether) occurred commonly in traditional aqueous sol-gel process [18]. Moreover, Pt(111)/Ti/SiO_2/Si substrates are adopted owing to their high stability and compatibility [11]. The SiO_2 layer serves as a barrier layer to reduce the leakage current density, while the Ti layer functions as a bonding layer to enhance the adhesion of the Pt(111) electrode onto the SiO_2 barrier layer.

2. Experimental details

2.1 Materials and synthesis process

The Pt(111)/Ti/SiO_2/Si substrates were prepared in-house. First, Si wafers were cleaned by a standard metal–oxide–semiconductor (MOS) cleaning process (i.e., the RCA clean) to remove organic contaminants, ionic contaminants, and native oxide layers, if any, thereby exposing a pure Si surface [19]. Second, a SiO_2 barrier layer of ~10 nm thickness was coated on the pure Si surface by oxidizing the cleaned Si wafers in an oxidation furnace at 1000 ℃ for 5 min. Finally, a Ti bonding layer of ~20 nm thickness and a Pt(111) electrode of ~120 nm thickness were deposited in sequence onto the as-prepared SiO_2/Si substrates in a sputtering chamber at 200 ℃ and 1.5 Pa for 2 and 10 min, respectively.

To prepare the NKBT precursor sol, tetrabutyl titanate ($Ti(OC_4H_9)_4$) (99%), bismuth nitrate ($Bi(NO_3)_3{\cdot}5H_2O$) (99.5%), sodium acetate ($NaCOOCH_3$) (99.5%), and potassium acetate ($KCOOCH_3$) (99%) were chosen as the raw materials, while isopropyl alcohol (99.5%), acetylacetone (99%), glacial acetic acid (99.8%), distilled water, and formamide (99.5%) were selected as the solvents. All chemicals were commercially acquired from Sinopharm Chemical Reagent Co., Ltd in China and were directly used without further purification. The whole preparation process was carried out under constant stirring in air and at room temperature in accordance with the desired composition of $(Na_{0.85}K_{0.15})_{0.5}Bi_{0.5}TiO_3$. First, $Ti(OC_4H_9)_4$, isopropyl alcohol, and acetylacetone were mixed at a weight ratio of 1 : 3 : 3, and glacial acetic acid was poured into the mixture at a volume ratio of 3 : 1 to form an initial solution. Second, $Bi(NO_3)_3{\cdot}5H_2O$ with a mole weight of 0.5 mol was introduced into the initial solution to give a slurry solution, and distilled water of the same volume as glacial acetic acid was added to dilute the slurry solution. Third, $NaCOOCH_3$ and $KCOOCH_3$ with mole weights of 0.425 and 0.075 mol were respectively applied to the diluted solution, and formamide was added at a volume ratio of 20 : 1 to prevent cracking during drying and annealing [7]. Finally, the resulting NKBT precursor sol, with a concentration of 0.26 M as determined by an inductively coupled plasma optical emission spectrometer (ICP-OES), was aged for ~10 days before being used in the synthesis of the NKBT multilayer thin films on the Pt(111)/Ti/SiO_2/Si substrates.

The synthesis procedure included spin coating, drying, pyrolysis, and annealing. First, spin coating of the aged NKBT precursor sol was employed to deposit one NKBT layer on

the Pt(111)/Ti/SiO_2/Si substrates using three different spin-coating conditions, including: (I) one-step spin coating at 4000 rpm for 30 s, (II) two-step (step 1/2) spin coating at 600/4000 rpm for 6/30 s, and (III) two-step (step 1/2) spin coating at 600/6000 rpm for 6/30 s. Second, each spin-coated NKBT layer was dried at 100 ℃ for 10 min and pyrolyzed at 450 ℃ for 5 min in an ambient atmosphere. Third, the above spin-coating, drying, and pyrolyzing procedure was repeated for 2–14 times to obtain NKBT multilayer thin films of 2–14 layers and with proportionally incremental thicknesses. Finally, the resulting NKBT/Pt/Ti/SiO_2/Si heterostructures were annealed by a rapid thermal processing (RTP) in oxygen ambient at 700 ℃ for 5 min under three different heating rate conditions of (I) 10 ℃/s, (II) 30 ℃/s, and (III) 70 ℃/s. The annealed NKBT/Pt/Ti/SiO_2/Si heterostructures were sputtered with Pt electrodes of 0.2 mm diameter to form the desired Pt/NKBT/Pt/Ti/SiO_2/Si heterostructure capacitor configuration. For ease of description, NKBT multilayer thin films of 2, 5, 8, 11, and 14 layers are denoted as NKBT-2, NKBT-5, NKBT-8, NKBT-11, and NKBT-14, respectively.

2.2 Structural and electromechanical evaluations

The phase structure of the NKBT multilayer thin films in the Pt/NKBT/Pt/Ti/SiO_2/Si heterostructures was examined by an X-ray diffractometer (XRD, D/MAX-RB, Rigaku, Japan) with CuKα radiation. The density was determined by the X-ray reflectometry (XRR) function in the XRD. The interfacial strain state was characterized by XRD ψ scan. The surface morphology, cross-sectional morphology, and thickness were acquired by a field emission scanning electron microscope (FESEM, LEO 1530, Carl Zeiss, Germany). The three-dimensional (3-D) surface morphology was observed by a scanning probe microscope (SPM, SPI4000&SPA300HV, Seiko, Japan) operating in atomic force microscopy (AFM) mode and equipped with an Rh-coated cantilever (SI-DF3) of a spring constant of 11 N/m and a free resonance frequency of 125 kHz. The detailed cross-sectional morphology was analyzed by a high-resolution transmission electron microscope (HRTEM, F20, Tecnai, USA). The phase change was studied by a Raman spectrometer (LabRAM HR800, Horiba, Japan) in back scattering geometry with a frequency resolution of 0.6 cm^{-1}. The chemical composition was obtained by an X-ray photoelectron spectroscope (XPS, PHI Quantera

SXM).

The ferroelectric properties were measured by a ferroelectric analyzer (TF Analyzer 2000, axiACCT, Germany). The dielectric properties were evaluated by a precision impedance analyzer (4294A, Agilent, USA). A power amplifier (603, Trek, USA) with the maximum output voltage of ±125 V was connected externally to the ferroelectric analyzer and the precision impedance analyzer to excite the NKBT multilayer thin films in the Pt/NKBT/Pt/Ti/SiO2/Si heterostructures at elevated electric field levels in the ferroelectric and dielectric property measurements. The piezoelectric properties were characterized by the SPM operating in contact atomic force microscopy (AFM) mode and equipped with an Rh-coated cantilever (SI-DF3-R) of a spring constant of 1.9 N/m and a free resonance frequency of 28 kHz. The ferroelectric polarization switching amplitude images and the hysteresis loops were measured by a piezoresponse force microscopy (PFM, MFP-3D Infinity, Oxford Instruments, United Kingdom) with conductive platinum-coated probe tips. The leakage current density was obtained using an electrometer (6517A Keithley, USA) and the power amplifier. The temperature-dependent dielectric property measurement was implemented using a temperature-controlled stage (THMS600, Guildford, UK).

3. Results and discussion

3.1 Effects of spin-coating and annealing conditions

The effect of spin-coating condition is first studied by keeping the annealing at 700 ℃ for 5 min under the optimized heating rate condition (II) of 30 ℃/s to be discussed in Fig. 3. Figure 1 shows the XRD patterns of three different NKBT-11 samples spin-coated with three different conditions of (I) one step at 4000 rpm for 30 s, (II) two steps (step 1/2) at 600/4000 rpm for 6/30 s, and (III) two steps (step 1/2) at 600/6000 rpm for 6/30 s. The two samples spin-coated with conditions (I) and (II), involving 4000 rpm for 30 s, exhibit a pure perovskite structure with no detection of secondary phase, irrespective of one or two step(s) of spin coating. For the one spin-coated with condition (III) at a higher speed of 6000 rpm, the appearance of a new diffraction peak at 2θ of ~30° is assigned to an undesirable pyrochlore phase. The largest peak at ~40° is due to the Pt(111) substrate electrode.

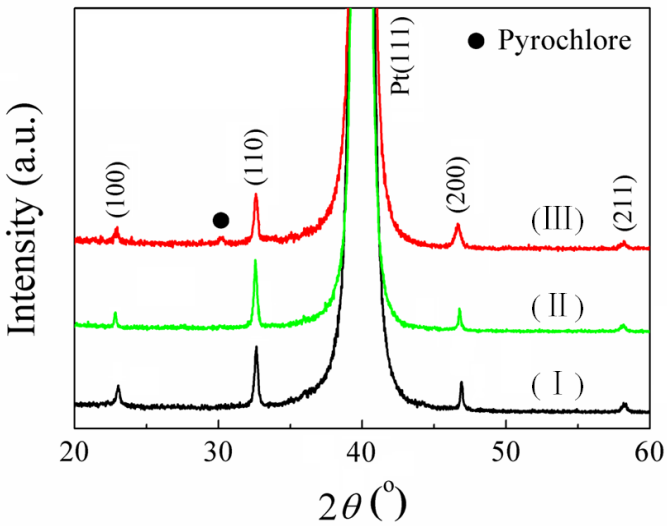

Fig. 1. XRD patterns of three different NKBT-11 samples spin-coated with three different conditions of (I) one step at 4000 rpm for 30 s, (II) two steps at 600/4000 rpm for 6/30 s, and (III) two steps at 600/6000 rpm for 6/30 s. A pyrochlore phase is detected for condition (III).

Figures 2(a) and 2(b) show the SPM–AFM 3-D surface morphological images of the two NKBT-11 samples spin-coated with the two best conditions (I) and (II) in Fig. 1, respectively. Figures 2(c) and 2(d) illustrate their corresponding XRD–XRR spectra. It is seen that the sample spin-coated with conditions (I) in Fig. 2(a) has a larger surface roughness than that spin-coated with condition (II) in Fig. 2(b). According to their XRD–XRR spectra in Figs. 2(c) and 2(d), the density of the samples spin-coated with conditions (I) and (II) is found to be 5.06 and 5.18 g/cm^3, respectively. Therefore, the use of spin-coating condition (II), i.e., two steps at 600/4000 rpm for 6/30 s, with annealing at 700 ℃ for 5 min under heating rate condition (II) of 30 ℃/s, is optimal for the synthesis of denser, uniformer, and purer perovskite NKBT multilayer thin films even though they are as thick as 11 layers.

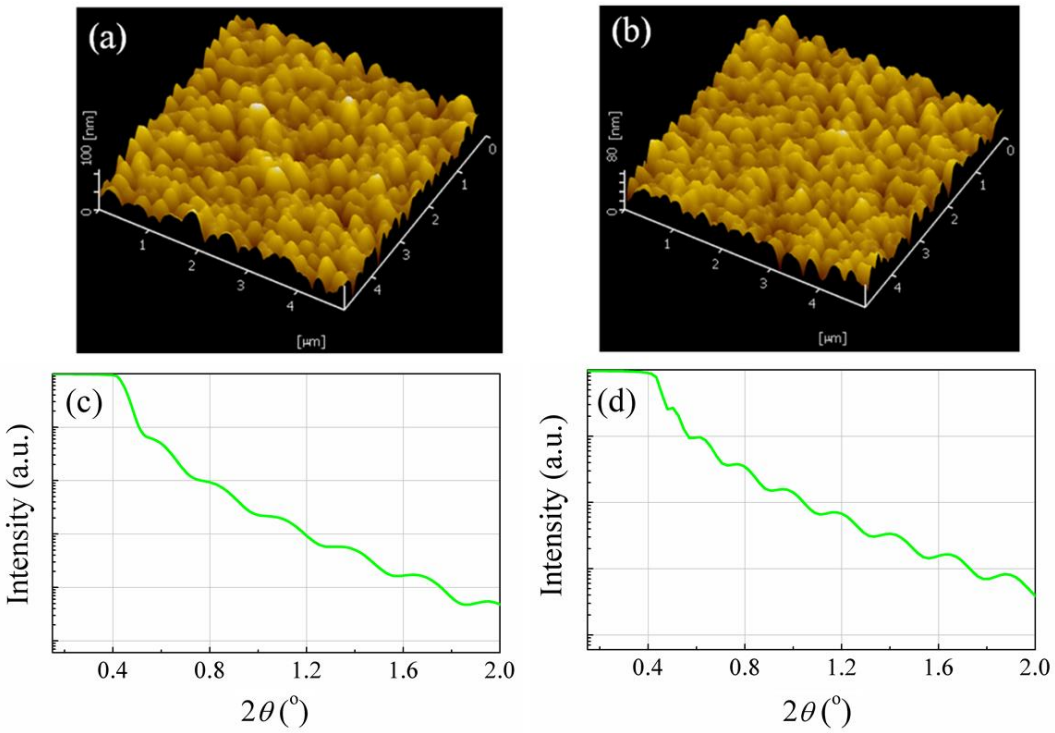

Fig. 2. SPM–AFM 3-D surface morphological images of NKBT-11 samples spin-coated with the two best conditions: (a) (I) and (b) (II). (c) and (d) are their corresponding XRD–XRR spectra.

After studying and optimizing the spin-coating condition in Figs. (1) and (2), the effect of annealing heating rate condition is now investigated by using the optimized spin-coating condition (II) of two steps at 600/4000 rpm for 6/30 s. Figure 3(a) gives the XRD patterns of three different NKBT-11 samples annealed at 700 ℃ for 5 min under three different heating rate conditions of (I) 10 ℃/s, (II) 30 ℃/s, and (III) 70 ℃/s. The two samples annealed with conditions (II) and (III) at higher heating rates of 30 and 70 ℃/s, respectively, are found to form a pure perovskite structure with no detection of secondary phase. However, condition (I) with a lower heating rate of 10 ℃/s results in an undesirable pyrochlore phase. Figures 3(b) and 3(c) display the FESEM surface morphological images of the samples annealed with the two best heating rate conditions (II) and (III), respectively. It is clear that heating rate condition (II) is more preferable to form a denser morphology with no obvious imperfections in comparison with condition (III). The occurrence of a relatively higher porosity in using condition (III) can be attributed to a more rapid volatilization of bismuth from the multilayer thin film surface at an elevated heating rate of 70 ℃/s. Therefore, annealing heating rate condition (II) of 30 ℃/s, when combined with spin-coating condition (II) of two steps at

600/4000 rpm for 6/30 s, is optimal for synthesizing denser, uniformer, and purer perovskite NKBT multilayer thin films.

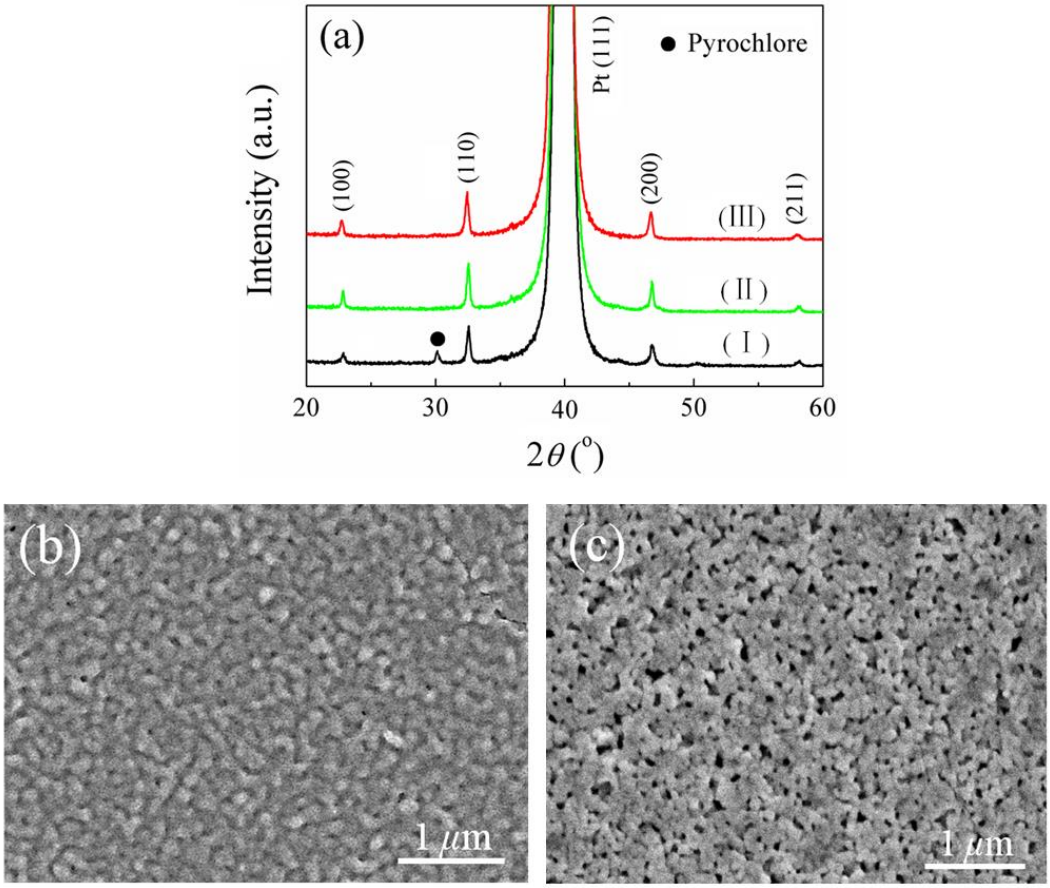

Fig. 3. (a) XRD patterns of three different NKBT-11 samples annealed at 700 °C for 5 min under three different heating rate conditions of (I) 10, (II) 30, and (III) 70 °C/s in which a pyrochlore phase is detected for condition (I). FESEM surface morphological images of the samples annealed with the two best heating rate conditions: (b) (II) and (c) (III).

3.2 Effect of multilayer thin film thickness on structural properties

With the optimized spin-coating and annealing conditions in Sec. 3.1, NKBT-2, NKBT-5, NKBT-8, NKBT-11, and NKBT-14 samples were synthesized, and the effect of multilayer thin film thickness on their structural properties is discussed in this section. Figures 4(a)–4(e) show the FESEM cross-sectional morphological images of all samples. The NKBT-2, NKBT-5, NKBT-8, and NKBT-11 samples in Figs. 4(a)–4(d) exhibit a consistently dense, uniform, and continuous morphology along their thickness direction with no obvious interfaces between different NKBT layers. Thus, the use of the optimized spin-coating and

annealing conditions in the modified aqueous sol-gel process is capable of synthesizing dense, uniform, and continuous NKBT multilayer thin films. By contrast, a clear interface, as marked by a red arrow in each image, is seen between the NKBT multilayer thin films and the Pt(111)/Ti/SiO_2/Si substrates for all samples in Figs. 4(a)–4(e). On the other hand, the NKBT-14 sample in Fig. 4(e) contains defects such as pinholes and cracks, as marked by red circles. Figure 4(f) plots the multilayer thin film thickness as a function of layer number for all samples. From the best-fit line, the thickness of our samples is found to increase quite linearly from ~100 nm for 2 layers (NKBT-2) to ~700 nm for 14 layers (NKBT-14). Therefore, the average thickness per layer in our samples is ~50 nm, and the maximum layer number and multilayer thin film thickness for preserving dense, uniform, continuous, and defect-free quality are 11 and ~550 nm, respectively; that is, the NKBT-11 sample. Figure 4(g) shows the HRTEM cross-sectional morphological image of the NKBT-11 sample on the basis of the FESEM image in Fig, 4(d). It is important to note that a thin interfacial layer of <5 nm thickness is observed to exist between the NKBT multilayer thin film and the Pt(111)/Ti/SiO_2/Si substrate for all samples in Figs. 4(a)–4(e), irrespective of their quality. This interfacial layer is mainly caused by the mismatch in both lattice parameters and thermal expansivity between the NKBT multilayer thin film and the Pt(111)/Ti/SiO_2/Si substrate during heat treatments [14–17]. Similar by-products, known as interfacial passive layers, have recently been observed in the Pt/$SrTiO_3$/Pt/MgO and Pt/$BaTiO_3$/LSCO/MgO heterostructures and found to have a significant impact on the electromechanical properties of the associated $SrTiO_3$ and $BaTiO_3$ thin films [14,15]. The influence of the interfacial passive layer on the electromechanical properties of our samples will be discussed in details in Secs. 3.3 and 3.4. Figure 4(h) displays the FESEM surface morphological image of the defective NKBT-14 sample in Fig. 4(e). It is in good agreement with Fig. 4(e) that pinhole-type defects (marked by red circles) are present in plane, besides along the thickness direction in Fig. 4(e). These defects will deteriorate the electromechanical properties of the NKBT-14 sample to be discussed in Sec. 3.3.

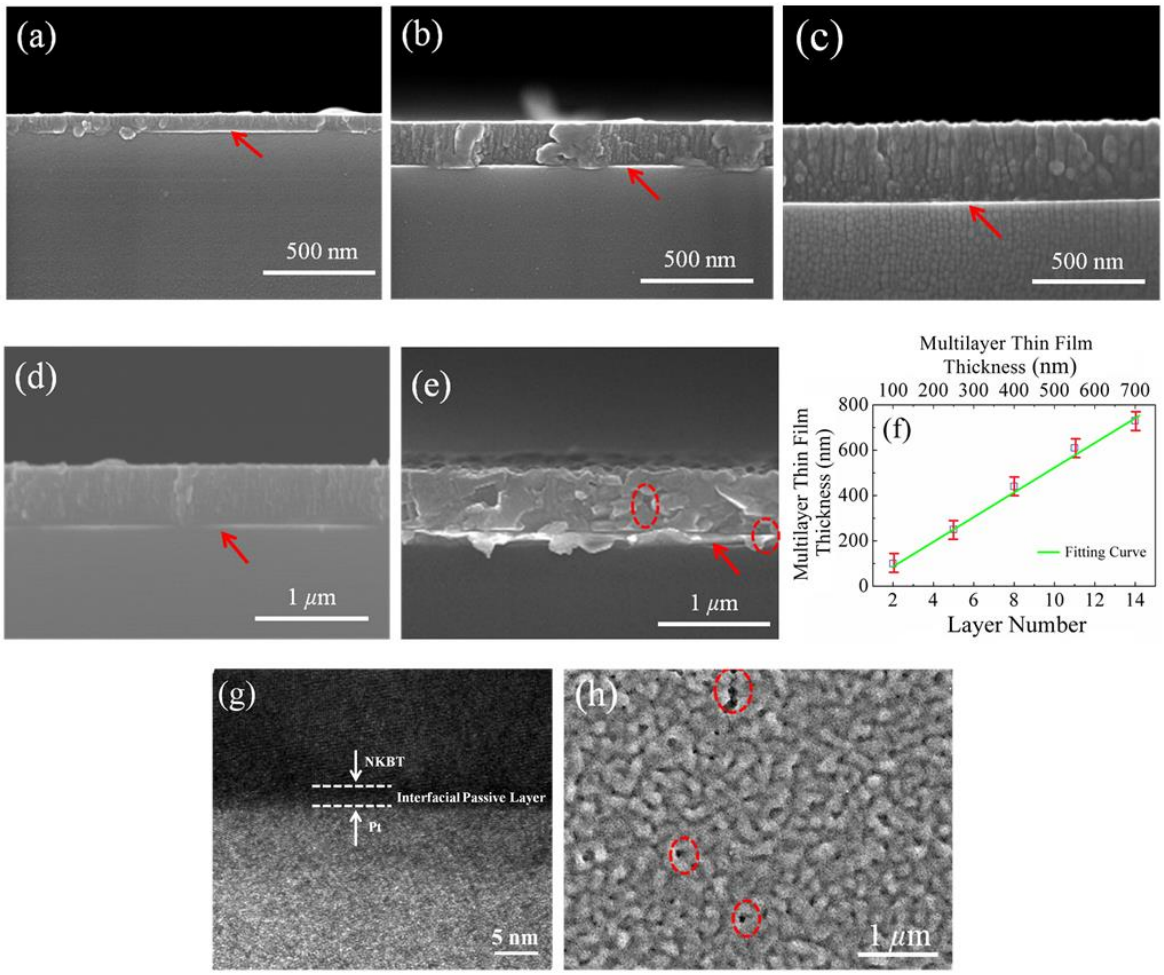

Fig. 4. FESEM cross-sectional morphological images of (a) NKBT-2, (b) NKBT-5, (c) NKBT-8, (d) NKBT-11, and (e) NKBT-14 samples. (f) Multilayer thin film thickness as a function of layer number. (g) HRTEM cross-sectional morphological image of NKBT-11 sample with an interfacial passive layer of <5 nm. (h) FESEM surface morphological image of NKBT-14 sample. The arrows indicate the interface between the NKBT multilayer thin films and the Pt(111)/Ti/SiO_2/Si substrates, while the circles mark the defects.

Figure 5(a) illustrates the XRD patterns of the NKBT-2, NKBT-5, NKBT-8, NKBT-11, and NKBT-14 samples. All samples show a desirable perovskite structure. The intensity of all diffraction peaks increases with increasing layer number (i.e., multilayer thin film thickness). The strongest peak comes from the (110) crystal plane. The intensity ratio of the (100) peak to the (110) peak is almost an invariant, indicating the presence of a very similar crystal structure in all samples with no preferential orientation (i.e., the crystal grains in the MLTHs grew in different orientations rather than in a preferred or specific orientation). By fitting the (100), (110), (200), and (211) peaks individually with Gaussian function and determining the total integrated intensity [1,20], the degree of relative crystallinity is found to

increase with increasing multilayer thin film thickness (not shown). Figure 5(b) gives the XRD step-scanned patterns in the 2θ range of 31–34°. The gradual upshift in the (110) peak toward the strain-free NKBT (110) peak (JCPDS 89-3109) with increasing multilayer thin film thickness implies a change in the interfacial strain state from relatively fixed in the thinner multilayer thin films to relatively free in the thicker multilayer thin films.

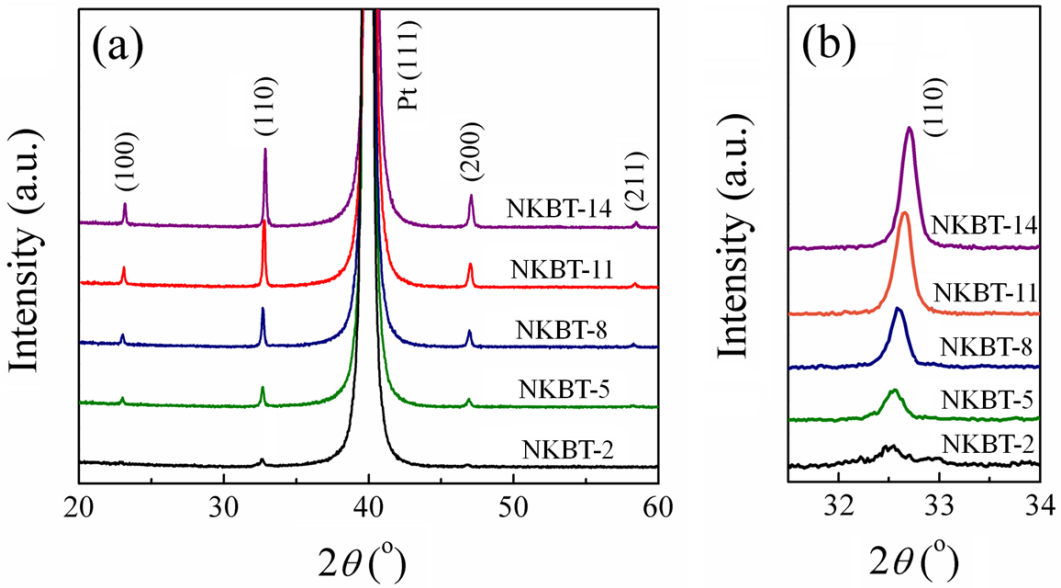

Fig. 5. (a) XRD patterns of NKBT-2, NKBT-5, NKBT-8, NKBT-11, and NKBT-14 samples. (b) XRD step-scanned patterns in the 2θ range of 31–34°.

In order to further investigate the thickness-induced change in the interfacial strain state, XRD ψ scan was performed on the diffraction of the (111) crystal plane of our NKBT samples. Here, we took the spacing of the (111) crystal plane of NKBT ceramic as the strain-free standard value for the evaluation of the interplanner spacing of the (111) crystal plane of our NKBT samples (d_ψ) at different tilt angles (ψ). The resulting d_ψ – $\sin^2\psi$ curves were used to analyze the residual strain on the basis of the Voigt model [21]. Figure 6 shows the d_ψ – $\sin^2\psi$ curves for the NKBT-2 and NKBT-11 samples. In both samples, d_ψ increases linearly with increasing $\sin^2\psi$, but the slope of the d_ψ – $\sin^2\psi$ curves decreases with increasing multilayer thin film thickness. The linear relationship between d_ψ and $\sin^2\psi$ indicates the existence of a strain state in the interfacial strain between the NKBT multilayer thin films and the Pt(111)/Ti/SiO_2/Si substrates, while the smaller slope in the thicker NKBT-11 compared

to the larger slope in the thinner NKBT-2 implies the presence of a lower interfacial strain state in the thicker NKBT-11 sample. Thus, the thickness-induced change in the interfacial strain state can be related to the interfacial passive layer in Fig. 4(g). More details will be described in Sec. 3.4, together with the effect of multilayer thin film thickness on the electromechanical properties to be reported in Sec. 3.3.

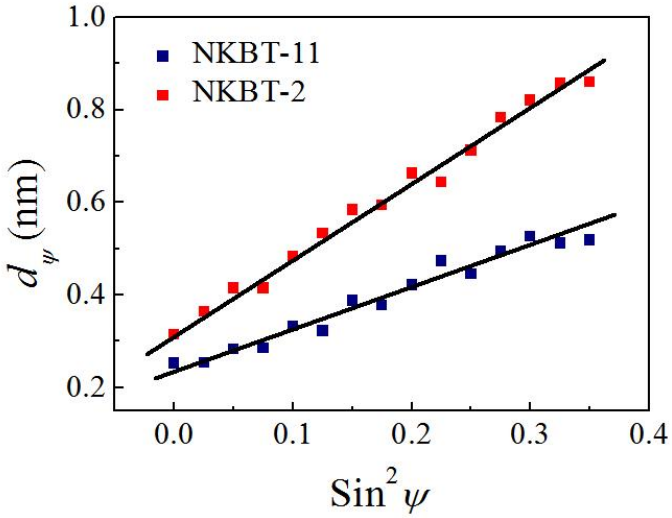

Fig. 6. d_ψ – $\sin^2\psi$ curves for NKBT-2 and NKBT-11 samples. The straight lines are the linearly fitted lines.

Figure 7 shows the XPS chemical composition depth profile of the NKBT-11 sample calibrated using C1s = 284.8 eV. The compositional distribution is homogeneous along the thickness direction, and the atomic ratio of (Na, K) : Bi : Ti : O corresponds closely to the stoichiometric $(Na, K)_{0.5}Bi_{0.5}TiO_3$. The transition of elements at the interface between the NKBT multilayer thin film and the Pt(111)/Ti/SiO_2/Si substrate occurs in a small time range. Therefore, the NKBT-11 sample, as an example, provides a proof of the existence of the stoichiometric and well-distributed composition in our samples.

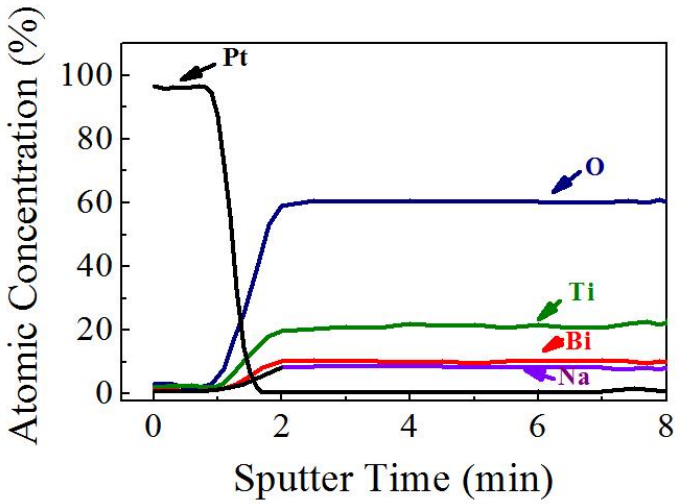

Fig. 7. XPS chemical composition depth profile of NKBT-11 sample calibrated using C1s = 284.8 eV.

To examine the temperature evolution of phase structure in our samples, the NKBT-11 sample was selected and characterized by the XRD in the temperature range of 20–200 ℃. As shown in Fig. 8(a), a pure perovskite structure with no detection of pyrochlore phase is obtained for temperature as high as 200 ℃. In perovskite materials, it is a common practice to distinguish between a rhombohedral phase and a tetragonal phase by noticing the split of the characteristic single rhombohedral (200) peak into two tetragonal (200) and (002) peaks in the 2θ range of 45–48° [22]. Since the chemical composition of our NKBT multilayer thin films is close to the rhombohedral–tetragonal MPB, a XRD step scan was employed to characterize the temperature evolution of phase structure in the 2θ range of 45–48°. As shown in Fig. 8(b), a single sharp (200) peak is seen in the step-scanned patterns at both 20 and 100 ℃, indicating the presence of a rhombohedral phase in our NKBT-11 sample. When the temperature is elevated to 140 ℃, the single sharp rhombohedral (200) peak splits into two peaks in which a (002) shoulder of the tetragonal phase appears in conjunction with the (200) peak. The splitting effect is more pronounced when the temperature is further elevated to 200 ℃. This reflects an increased contribution from the tetragonal phase. Therefore, there exists a rhombohedral–tetragonal phase transition at ~140 ℃ in our NKBT-11 sample.

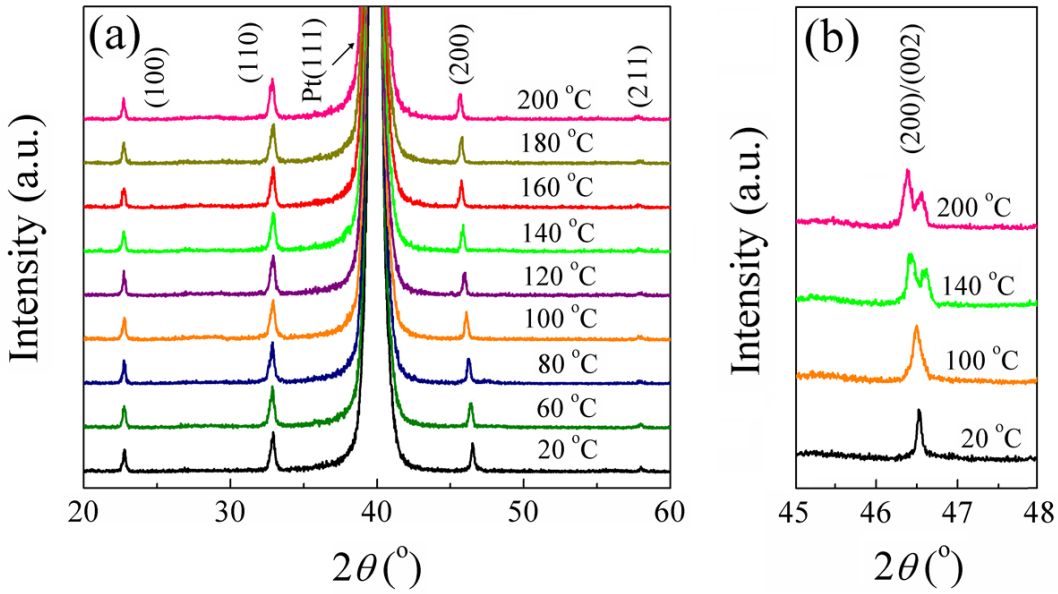

Fig. 8. (a) XRD patterns of NKBT-11 sample in the temperature range of 20–200 °C. (b) XRD step-scanned patterns in the 2θ range of 45–48° at different temperatures.

Figure 9 provides the Raman spectra of the NKBT-11 sample in Fig. 8 at different temperatures in order to further confirm the observed phase change. Three Raman peaks, including A_1(2TO), E(3TO), and A_1(3TO) and corresponding to the tetragonal phase, appear in the Raman spectra when the temperature is increased to 140 and 200 °C [23–25]. Moreover, the small peak detected at ~135 cm^{-1} (no label) at both 20 and 100 °C are assigned to a Raman mode of rhombohedral symmetry. This peak is weakened with an increase in temperature and disappears at 140 °C. Therefore, the Raman study further confirms the rhombohedral–tetragonal phase transition at ~140 °C in our NKBT-11 sample. This phase transition temperature also agrees with the previously reported NKBT ceramic and single-layer thin film [3,5,6].

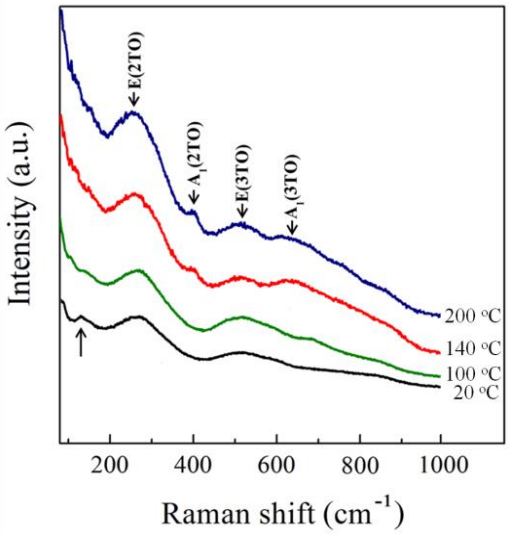

Fig. 9. Raman spectra of NKBT-11 sample in Fig. 8 at different temperatures.

3.3 Effect of multilayer thin film thickness on electromechanical properties

The effect of multilayer thin film thickness on the electromechanical properties of the NKBT-2, NKBT-5, NKBT-8, NKBT-11, and NKBT-14 samples are explored in this section. These include the ferroelectric, dielectric, piezoelectric, and electric properties.

3.3.1 Ferroelectric properties

Figure 10 shows the ferroelectric properties of all samples at room temperature. The ferroelectric hysteresis loops of all samples in Fig. 10(a) were measured under an AC applied field of 750 kV/cm peak at 100 Hz, while those of the NKBT-11 sample in Fig. 10(b) were acquired under different AC applied field levels of 350, 550, 750, and 900 kV/cm peak at 100 Hz. The results in Figs. 10(a) and 10(b) represent the 2nd cycle data. In Fig. 10(a), all samples, including NKBT-2 of as less as 2 layers and as thin as ~100 nm, exhibit typical and saturated ferroelectric hysteresis loops without breakdown even subjected to a high AC applied field of 750 kV/cm peak. In Fig. 10(b), the ferroelectric hysteresis loops of the NKBT-11 sample can be readily enlarged by gradually increasing the AC applied field level to 900 kV/cm peak. These reflect the good high-field withstandability of our samples. In Fig. 10(c), the remnant polarization (P_r), saturation polarization (P_s), and coercive field (E_c) of all samples are extracted from Fig. 10(a) and plotted as a function of both layer number and multilayer thin film thickness. It is clear that P_r and P_s increase, while E_c decreases, with increasing layer number from 2 to 11, corresponding to increasing multilayer thin film

thickness from ~100 to ~550 nm. The NKBT-11 sample demonstrates the highest P_r of 18.3 μC/cm^2 and P_s of 53.6 μC/cm^2, together with the lowest E_c of 116 kV/cm, under 750 kV/cm peak AC applied field. P_r of our NKBT-11 sample is much superior to the NKBT films of similar thickness prepared by Yu. *et al.* (P_r = 13.8 μC/cm^2) and Chi *et al.* (P_r = 12.5 μC/cm^2) using traditional sol-gel method [6,10] as well as by Dong *et al.* (P_r = 8.9 μC/cm^2) using other method [26]. The fact that the NKBT-14 sample of ~700 nm thickness has weaker ferroelectric properties compared to the NKBT-11 sample is the presence of defects as shown in Figs. 4(e) and 4(h) (marked by red circles). Nonetheless, these thickness-dependent improvement in ferroelectric properties in conjunction with the thickness-induced change in the interfacial strain state in Figs. 5 and 6, are a result of the interfacial passive layer appeared between the multilayer thin film and the substrate in Fig. 4(g) [14–17].

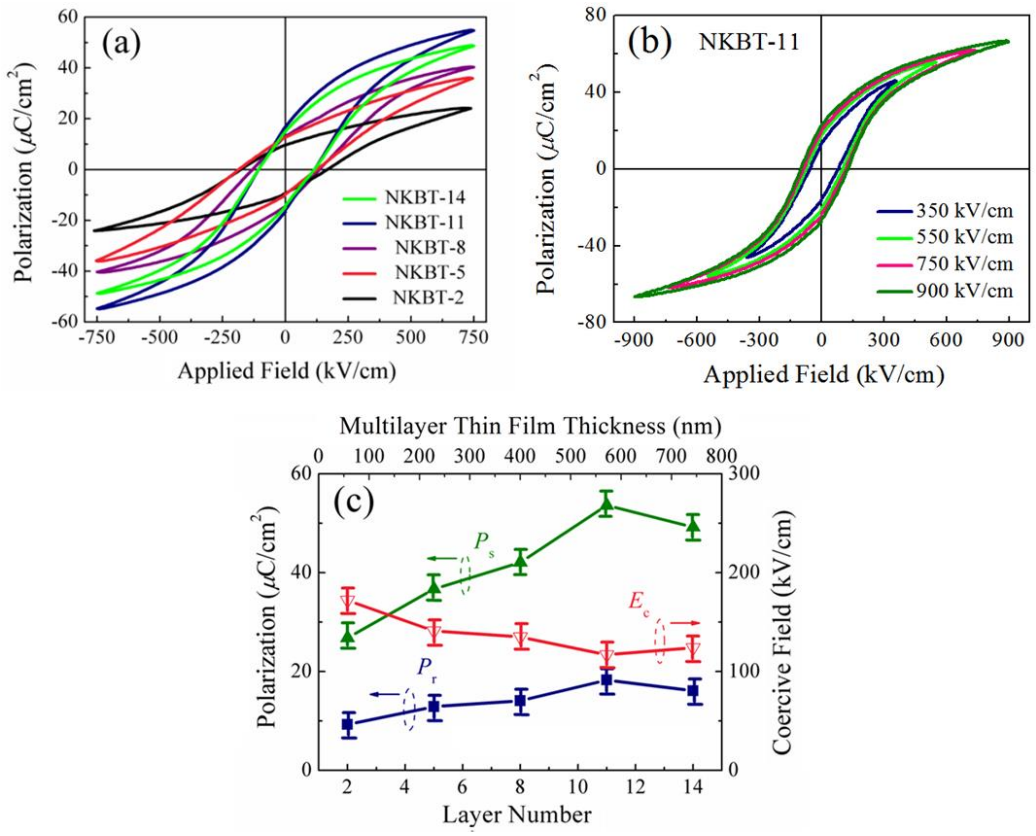

Fig. 10. Ferroelectric properties of NKBT-2, NKBT-5, NKBT-8, NKBT-11, and NKBT-14 samples at room temperature. (a) Ferroelectric hysteresis loops of all samples under an AC applied field of 750 kV/cm peak at 100 Hz. (b) Ferroelectric hysteresis loops of NKBT-11 sample under different AC applied field levels at 100 Hz. (c) Remnant polarization (P_r), saturation polarization (P_s), and coercive field (E_c) extracted from (a) as a function of both layer number and multilayer thin film thickness.

3.3.2 Dielectric properties

Figure 11 shows the dielectric properties of all samples at room temperature. These include the dependence of relative dielectric constant (ε_r) and loss tangent (tanδ) on frequency for all samples in Fig. 11(a), that on AC applied field for some selected samples at 100 kHz in Fig. 11(b), and that on both layer number and multilayer thin film thickness in Fig. 11(c). The values of ε_r and tanδ in Fig. 11(c) are extracted from Fig. 11(b) at 0 kV/cm applied field. It is seen that ε_r increases, while tanδ decreases, with increasing layer number from 2 to 11 or multilayer thin film thickness from ~100 to ~550 nm. The NKBT-11 sample demonstrates the best dielectric properties with the highest ε_r of 463 and the lowest tanδ of 0.057. The defects in the NKBT-14 sample lead to a lower ε_r and a higher tanδ. From Fig. 11(b), the samples exhibit ferroelectric-type butterfly curves for both ε_r and tanδ versus applied field, suggesting the presence of field-induced domain-wall motion in the samples. In agreement with the thickness-dependent improvement in ferroelectric properties in Sec. 3.3.1, our NKBT-11 sample has dielectric properties superior to the NKBT films reported by Yu *et al.* (ε_r = 360, tanδ = 0.059) using traditional sol-gel method [6]. Recalling that the reversible polarization (P) of ferroelectric thin films can be related to ε_r by:

$$P = t\varepsilon_0 \int_{-E_m}^{E_m} \varepsilon_r(E)dE \quad (1)$$

where t is the thin-film thickness, E_m is the maximum applied field, and ε_0 is the dielectric constant of free space [27]. P in Eq. (1) has a proportional relationship with both t and ε_r. This means that both P_r and P_s increase with increasing multilayer thin film thickness, in agreement with the observation in Fig. 10. Moreover, when ε_r is increased, both P_r and P_s are also increased, agreed with Fig. 11. Therefore, these thickness-dependent dielectric properties have a close relationship with the thickness-dependent ferroelectric properties in Fig. 10 which, in turn, can be related to the interfacial passive layer in Fig. 4(g).

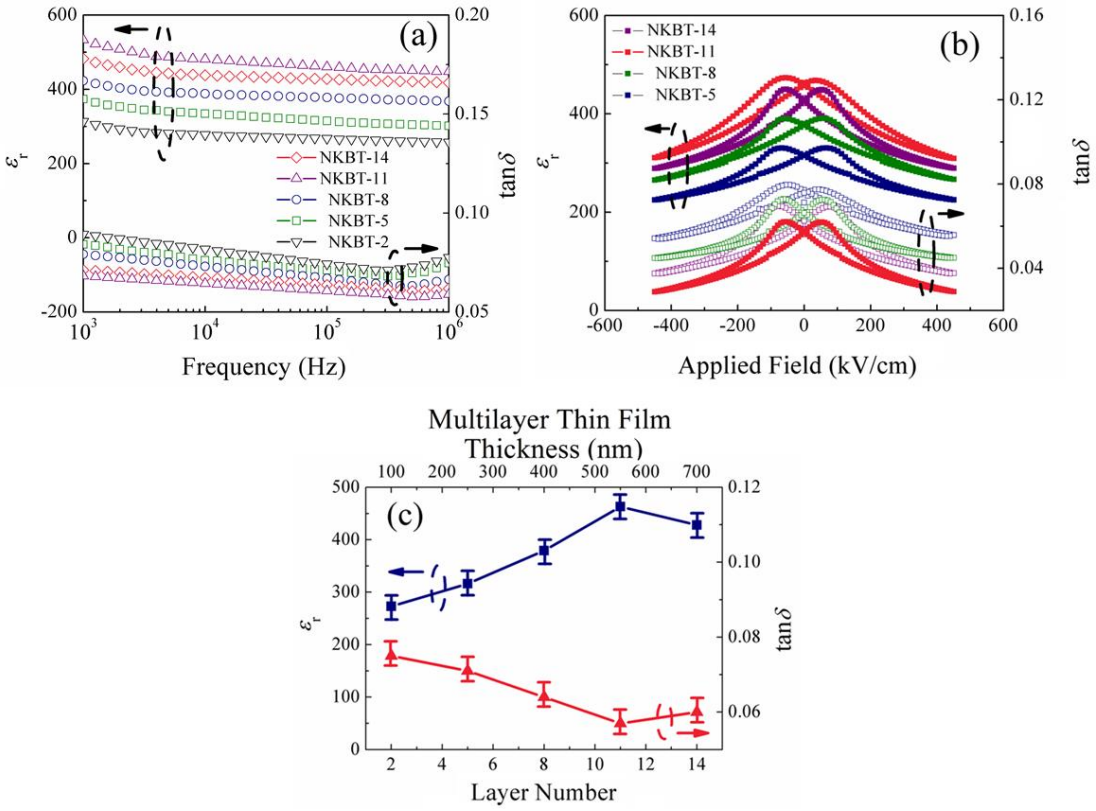

Fig. 11. Dielectric properties of NKBT-2, NKBT-5, NKBT-8, NKBT-11, and NKBT-14 samples at room temperature. Dependence of dielectric constant (ε_r) and loss tangent (tanδ) on (a) frequency, (b) applied field, and (c) layer number and multilayer thin film thickness.

Since an interfacial passive layer can be modeled as a parasitic interfacial capacitor in series with the interior of the multilayer thin film [14,15], the total capacitance of our Pt/NKBT/Pt/Ti/SiO_2/Si heterostructure (C_H) can be expressed as:

$$1/C_H = 1/C_{MLTH} + 1/C_{IPL} + 1/C_{Sub} \quad (2)$$

where C_{MLTH}, C_{IPL}, and C_{Sub} are the capacitance of the multilayer thin film, the interfacial passive layer, and the substrate, respectively. As our heterostructure has a circular top electrode of 0.2 mm diameter, each capacitance in Eq. (2) can be assumed as a planar capacitance with the same area (S), and Eq. (2) becomes:

$$S/C_H = t_{MLTH}/\varepsilon_o\varepsilon_{rMLTH} + t_{IPL}/\varepsilon_o\varepsilon_{rIPL} + S/C_{Sub} \quad (3)$$

where t_{MLTH} and t_{IPL} are the thicknesses of the multilayer thin film and interfacial passive layer, respectively; and ε_{rMLTH} and ε_{rIPL} are the relative dielectric constants of the multilayer thin film and interfacial passive layer, respectively. Since the top and bottom Pt electrodes of the heterostructure were used as the electrical leads for dielectric measurements, the effect of C_{Sub} in Eqs. (2) and (3) is small and can be neglected. As the interfacial passive layer is very

thin (i.e., t_{IPL} < 5 nm in Fig. 4(g)) in comparison with the multilayer thin films of 100–700 nm, t_{MLTH} can be assumed to be the effective thickness of the heterostructure. Thus, S/C_{H} in Eq. (3) can be plotted as a function of t_{MLTH} using the results of Fig. 11(c). As shown in Fig. 12, S/C_{H} has a linear function with t_{MLTH} and a nonzero *y*-intercept, suggesting the presence of an interfacial passive layer in our heterostructure [28]. The relatively large deviation for the NKBT-14 sample is owing to the defects.

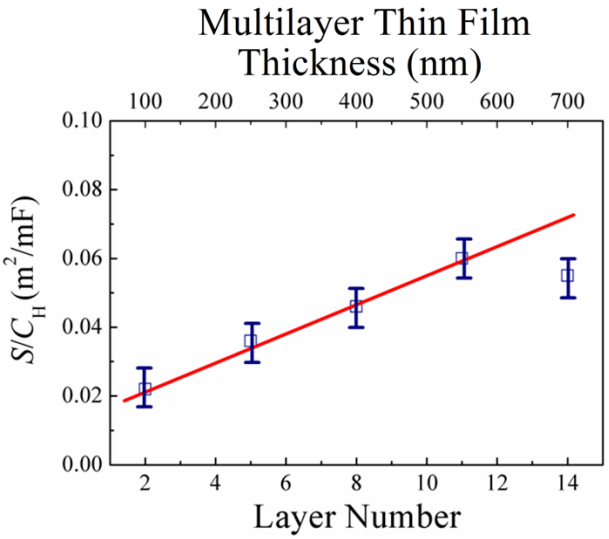

Fig. 12. S/C_{H} as a function of layer number or multilayer thin film thickness (t_{MLTH}). The straight line is the linearly fitted line.

3.3.3 Piezoelectric properties

Figure 13 shows the piezoelectric properties of all samples at room temperature. The displacement–field curves in Fig. 13(a) were measured under an AC applied field of 200 kV/cm peak at 100 Hz. The strain–field curves in Fig. 13(b) are obtained from the maximum displacement values as in Fig. 13(a) at different AC applied field levels. The effective piezoelectric coefficients (d_{33}^{*}) and the maximum strain in Fig. 13(c) are extracted from the slope and strain at 200 kV/cm of the strain–field curves of Fig. 13(b), respectively. In Fig. 13(a), the butterfly-like displacement–field curves not only confirm the ferroelectric nature of our samples, but also elucidate the field-induced motion of non-180° domain walls as well as its contribution to the reversible polarization discussed in Eq. (1) [29]. In Fig. 13(c), d_{33}^{*} and maximum strain show similar quantitative trends in layer number (or multilayer thin film thickness) to P_{r} and P_{s} in Fig. 10(c) as well as to ε_{r} in Fig. 11(c). Again, the NKBT-11 sample

possesses the best piezoelectric properties in terms of the largest d_{33}^* of 64 pm/V and maximum strain of 0.17%. The d_{33}^* value of the NKBT-11 sample is comparable to the NKBT films obtained in a previous study [25]. The general property reduction in the NKBT-14 sample is due to the defects (Figs. 4(e) and 4(h)). In fact, d_{33}^* can be expressed in terms of P and ε_r as follows:

$$d_{33}^* = 2\varepsilon_r PQ \tag{4}$$

where P can be approximated by P_r (Fig. 10) and Q is the electrostriction coefficient in relation to the initial strain state (relatively fixed or free) of the multilayer thin films (Fig. 5) [30]. Therefore, it can reasonably explain why d_{33}^* has an increasing trend with increasing layer number or multilayer thin film thickness. This also points out the existence of interfacial passive layer effect on the thickness-dependent structural, ferroelectric, dielectric, and piezoelectric properties.

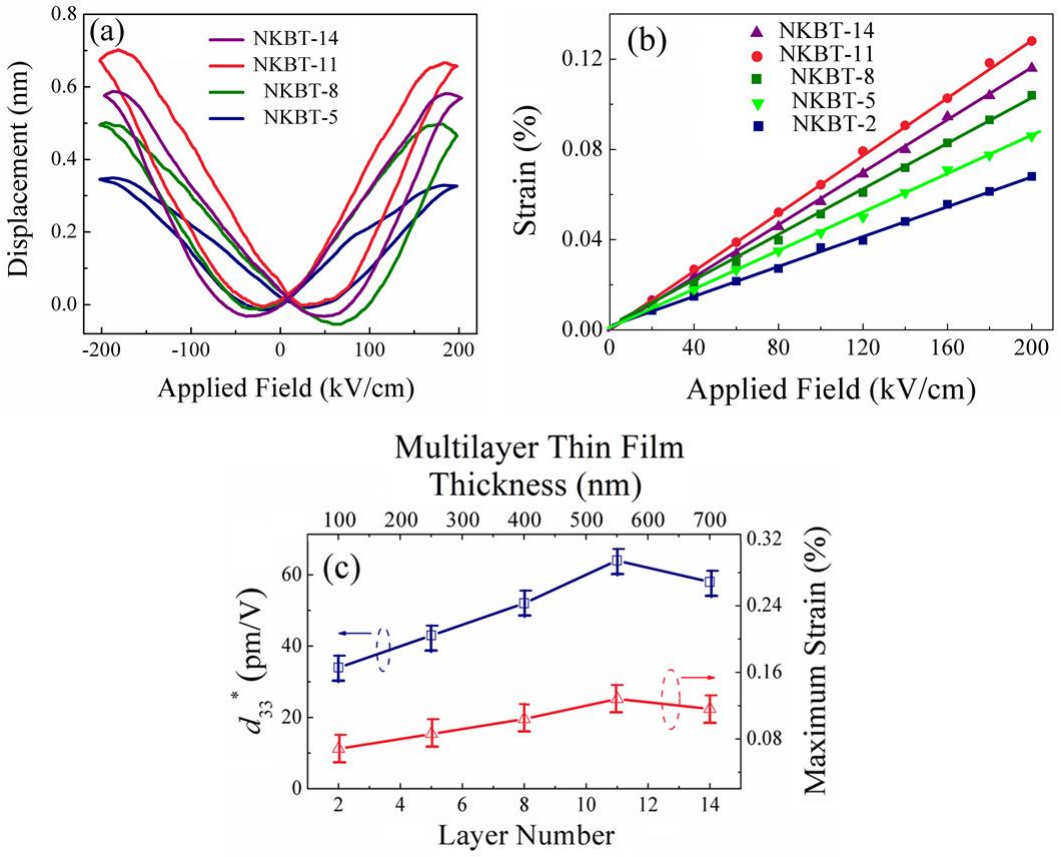

Fig. 13. Piezoelectric properties of NKBT-2, NKBT-5, NKBT-8, NKBT-11, and NKBT-14 samples at room temperature. (a) Displacement–field curves. (b) Strain–field curves. (c) Effective piezoelectric coefficients (d_{33}^*) and maximum strain as a function of both layer number and multilayer thin film thickness.

PFM was employed to investigate the ferroelectric domain patterns and switching of our NKBT samples in order to have a deeper understanding of the thickness-dependent interfacial passive layer effect. A graphic pattern with a negative bias of −20 V on the outer square ring and a positive bias of +20 V on the inner square ring was applied to the NKBT samples with the probe being grounded. Figures 14(a) and 14(b) show the ferroelectric polarization switching amplitude images of the NKBT-2 and NKBT-11 samples, respectively. It is seen that domain reversal is only partially induced in the NKBT-2 sample, but most of the domain reversal is induced in the NKBT-11 sample. The more induced domain switching in the thicker NKBT-11 sample is ascribed to the enhanced domain mobility due to the lowered constraint by the interfacial passive layer. By fixing the probe tip on the surface of the assembly and applying a negative–positive bias voltage from −20 to +20 V, the hysteresis loops in amplitude and phase versus voltage were recorded. In Fig. 14(c), the thicker NKBT-11 sample exhibits typical “butterfly” hysteresis loops, which not only indicate large ferroelectric polarization switching behavior but also manifest the smaller impact of the interfacial passive layer on the domain mobility. That is, more domain switching is possible under applied fields.

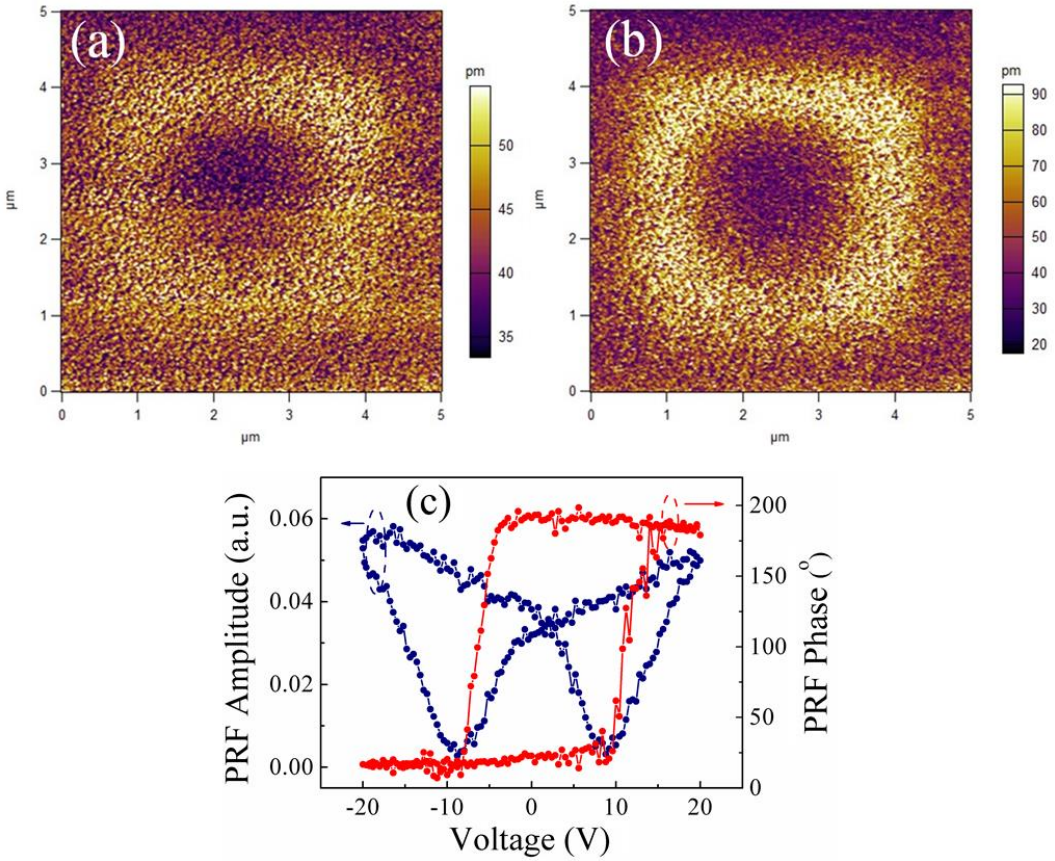

Fig. 14. Ferroelectric polarization switching amplitude images of (a) NKBT-2 and (b) NKBT-11; (c) Hysteresis loops in amplitude and phase versus voltage of NKBT-11 sample.

3.3.4 Electric properties

The leakage current density is an essential electric property for using the NKBT multilayer thin film-based heterostructures in high-performance devices, especially for power devices. Figure 15(a) plots the applied field dependence of leakage current density for all samples at room temperature, while Fig. 15(b) shows the maximum leakage current density obtained at 400 kV/cm as a function of both layer number and multilayer thin film thickness. Agreed with the previous observations in Figs. 10, 11, and 13 for the ferroelectric, dielectric, and piezoelectric properties, the NKBT-11 sample demonstrates the lowest leakage current density of 2.7×10^{-5} A/cm^2 and is mainly attributed to the reduction of oxygen vacancies or other charged defects at the interface between the multilayer thin film and the substrate.

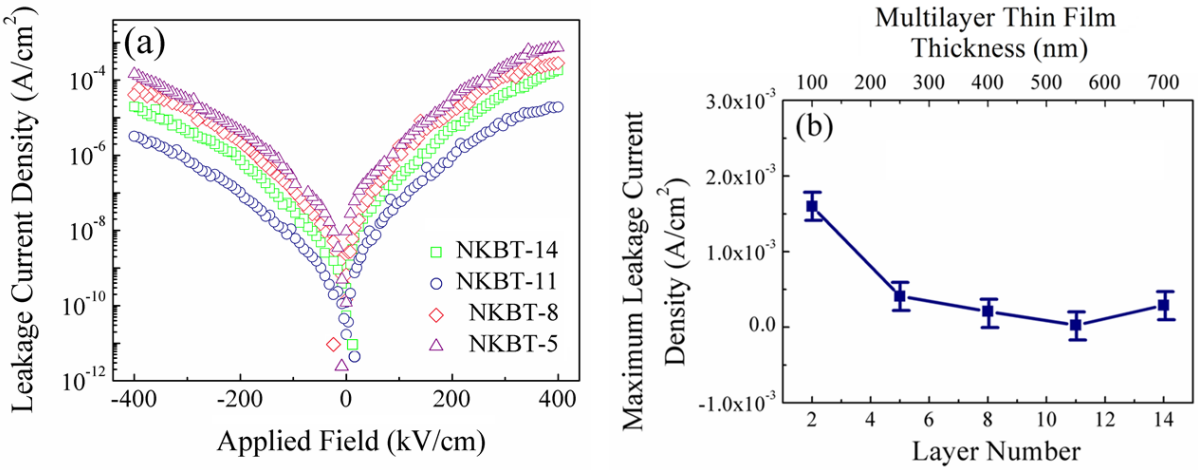

Fig. 15. (a) Applied field dependence of leakage current density of NKBT-5, NKBT-8, NKBT-11, and NKBT-14 samples at room temperature. (b) Maximum leakage current density obtained at 400 kV/cm as a function of both layer number and multilayer thin film thickness.

3.4 Thickness-dependent interfacial passive layer effect

In this section, we consolidate several important observations and analytical results, including: (1) the interfacial passive layer in Fig. 4(g); (2) the thickness-induced change in the interfacial strain state from relatively fixed to relatively free with increasing multilayer thin film thickness in Figs. 5 and 6; and (3) the thickness-dependent improvement in the ferroelectric, dielectric, piezoelectric, and electric properties in Sec. 3.3. Figure 16 illustrates the schematic diagram of our Pt/NKBT/Pt/Ti/SiO_2/Si heterostructure with an interfacial passive layer between the NKBT multilayer thin film and the Pt(111)/Ti/SiO_2/Si substrate. Since the interfacial passive layer is a result of the mismatch in lattice parameter and thermal expansivity between the multilayer thin film and the substrate during heat treatments, it generally accompanies with in-plane misfit strains which, in turn, tend to constrain the motion of non-180^o domain walls of the multilayer thin film [31,32]. These interfacial in-plane misfit strains also act as potential wells to trap charged defects such as oxygen vacancies upon an applied electric field [33,34]. The trapped charged defects are equivalent to domain-pinning centers to constrain both the 180^o and non-180^o domain-wall motions in the multilayer thin film near the interface. When the multilayer thin film is thin enough, most of the domains will be close to the interfacial passive layer and subject to its relatively high interfacial strain state. By increasing the multilayer thin film thickness, the number of domains available in the upper part of the multilayer thin film will increase in respect to the

lower interfacial strain state in the thicker multilayer thin films, giving rise to an increased motion of domain walls under fields. Therefore, the structural and electromechanical properties exhibit consistent increasing trends with increasing layer number from 2 to 11 or multilayer thin film thickness from 100 to 550 nm.

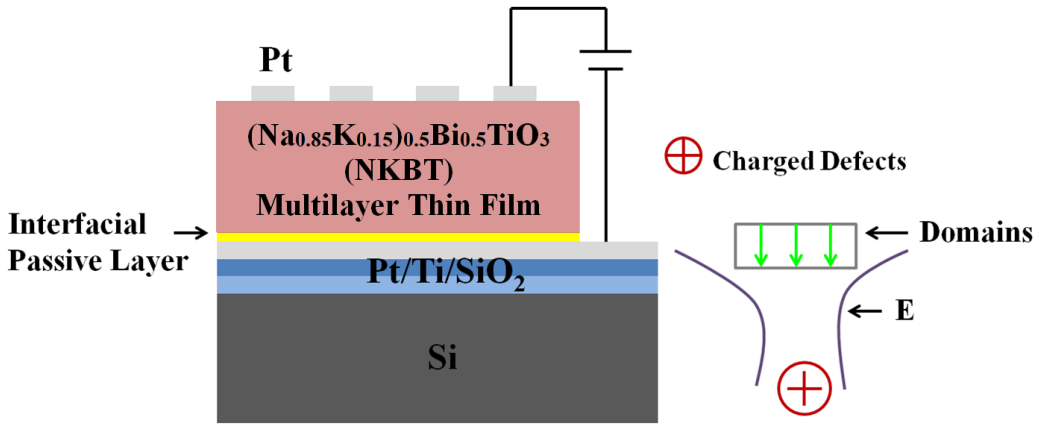

Fig. 16. Schematic diagram of Pt/NKBT/Pt/Ti/SiO_2/Si heterostructure with an interfacial passive layer.

To further analyze the interfacial passive layer and its thickness-dependent effect on domain pinning and domain-wall motion, the dependence of applied field on dielectric constant (ε_r) of all samples were measured at both room temperature and -160 ^oC, and the measured ε_r values were normalized by the zero-field dielectric constant (ε_{rzero}) as shown in Fig. 17. By best fitting the measured curves, the normalized dielectric constant ($\varepsilon_r/\varepsilon_{rzero}$) of all samples at different temperatures show linearly increasing tends with applied field in accordance with the Rayleigh relation expressed as follows:

$$\varepsilon_r/\varepsilon_{rzero}=1+\alpha E \quad (5)$$

where α is the Rayleigh coefficient and is the slope of the curves. α provides an indicator for characterizing the nonlinearity of the dielectric response [35]. It is clear that α increases with increasing layer number or multilayer thin film thickness even at temperature as low as -160 ^oC. This indicates an increased contribution from domain-wall motion by weakening the influence of domain pinning in the thicker multilayer thin films.

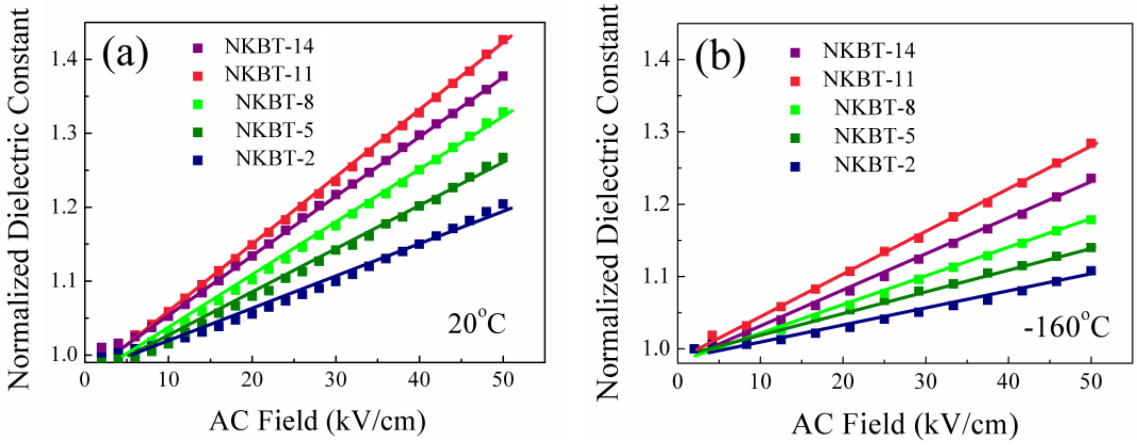

Fig. 17. Dependence of applied field on normalized dielectric constant for NKBT-2, NKBT-5, NKBT-8, NKBT-11, and NKBT-14 samples at (a) 20 and (b) -160 °C.

4. Conclusion

We have synthesized NKBT multilayer thin films with the composition of $(Na_{0.85}K_{0.15})_{0.5}Bi_{0.5}TiO_3$, the average layer thickness of ~50 nm, and five different layer numbers of 2, 5, 8, 11, and 14 to give five different multilayer thin film thicknesses of about 100, 250, 400, 550, and 700 nm on Pt(111)/Ti/SiO_2/Si substrates to form five different types of Pt/NKBT/Pt/Ti/SiO_2/Si heterostructure samples using a modified aqueous sol-gel process. We have studied the synthesis process using different combinations of spin-coating and annealing heating rate conditions and have optimized spin-coating condition (II) of two steps at 600/4000 rpm for 6/30 s with annealing heating rate condition (II) of 30 °C/s for the synthesis of dense, uniform, continuous, and pure perovskite NKBT multilayer thin films up to 11 layers. Based on the optimized process conditions, we have investigated the thickness-dependent structural and electromechanical (i.e., ferroelectric, dielectric, piezoelectric, and electric) properties of the NKBT multilayer thin films in the heterostructures. The NKBT multilayer thin films of different thicknesses have shown a pure perovskite structure with a rhombohedral–tetragonal phase transition at ~140 °C and no preferential orientation. Their structural and electromechanical properties have exhibited consistent increasing trends with increasing layer number of 2–11 or multilayer thin film thickness of 100–550 nm. The 550 nm-thick, 11-layer multilayer thin films have demonstrated the best structural and electromechanical properties. An interfacial passive layer has been observed at the interface between the multilayer thin films and the substrates. The effect of the interfacial passive layer

on the thickness-dependent property improvement in the NKBT multilayer thin film-based heterostructures has been studied and ascribed to the enhanced motion of both 180º and non-180º domain walls in the thicker multilayer thin films by weakening the contribution of domain pinning in the interfacial passive layers. The present work provides a guide to the design and applications of ferroelectric, dielectric, and piezoelectric multilayer thin film-based heterostructures.

Acknowledgments

This work was supported by the Innovation and Technology Commission of the HKSAR Government to the Hong Kong Branch of National Rail Transit Electrification and Automation Engineering Technology Research Center (1-BBYW), the Research Grants Council of the HKSAR Government (522813), and the National Science Foundation of China (51402020).

Author Contributions

Yunyi Wu performed both the theoretical and experimental work. Siu Wing Or conceived the project and guided Yunyi in the whole work.

References

[1] K. Roleder, I. Franke, A.M. Glazer, P.A. Thomas, S. Miga, J. Suchanicz, The piezoelectric effect in $Na_{0.5}Bi_{0.5}TiO_3$ ceramics, J. Phys.: Condens. Matter 14 (2002) 5399–5406.

[2] V.A. Isupov, Ferroelectric $Na_{0.5}Bi_{0.5}TiO_3$ and $K_{0.5}Bi_{0.5}TiO_3$ perovskites and their solid solutions, Ferroelectrics 315 (2005) 123–147.

[3] K. Yoshii, Y. Hiruma, H. Nagata, T. Takenaka, Electrical properties and depolarization temperature of $(Bi_{1/2}Na_{1/2})TiO_3$–$(Bi_{1/2}K_{1/2})TiO_3$ lead-free piezoelectric ceramics, Jpn. J. Appl. Phys. 45 (2006) 4493–4496.

[4] M. Izumia, K. Yamamoto, M. Suzuki, Y. Noguchi, M. Miyayama, Large electric-field-induced strain in $Bi_{0.5}Na_{0.5}TiO_3$–$Bi_{0.5}K_{0.5}TiO_3$ solid solution single crystals, Appl. Phys. Lett. 93 (2008) 242903.

[5] A. Moosavi, M.A. Bahrevar, A.R. Aghaei, P. Ramos, M. Algueró, H. Amorín, High-field electromechanical response of $Bi_{0.5}Na_{0.5}TiO_3$–$Bi_{0.5}K_{0.5}TiO_3$ across its morphotropic phase boundary, J. Phys. D: Appl. Phys. 47 (2014) 055304.

[6] T. Yu, K.W. Kwok, H.L.W. Chan, The synthesis of lead-free ferroelectric $Bi_{0.5}Na_{0.5}TiO_3$-$Bi_{0.5}K_{0.5}TiO_3$ thin films by sol-gel method, Mater. Lett. 61 (2007) 2117–2120.

[7] Y.Y. Wu, X.H. Wang, C.F. Zhong, L.T. Li, Effect of Na/K excess on the electrical properties of $Na_{0.5}Bi_{0.5}TiO_3$–$K_{0.5}Bi_{0.5}TiO_3$ thin films prepared by sol-gel processing, Thin Solid Films 519 (2011) 4798–4803.

[8] X.J. Zheng, J.Y. Liu, J.F. Peng, X. Liu, Y.Q. Gong, K.S. Zhou, D.H. Huang, Effect of potassium content on electrostrictive properties of $Na_{0.5}Bi_{0.5}TiO_3$-based relaxor ferroelectric thin films with morphotropic phase boundary, Thin Solid Films 548 (2013) 118–124.

[9] W. Cui, X. Wang, L. Li, Large piezo response of $Na_{0.5}Bi_{0.5}TiO_3$–$K_{0.5}Bi_{0.5}TiO_3$ thin films prepared via water-based sol-gel method, Ceram. Int. 41 (2015) S37–S40.

[10] Q.G. Chi, J.F. Dong, C.H. Zhang, Y. Chen, X. Wang, Q.Q. Lei, A simple, low-temperature fabrication method of highly (100)-oriented $(Na_{0.85}K_{0.15})_{0.5}Bi_{0.5}TiO_3$ thin films with outstanding electric properties, J. Alloy. Compd. 704 (2017) 336–342.

[11] H.W. van Zeijl, Thin film technologies for micro/nano systems; a review, ECS Trans. 61 (2014) 191–206.

[12] C. Basceri, S.K. Streiffer, A. I. Kingon, R. Waser, The dielectric response as a function of

temperature and film thickness of fiber-textured (Ba,Sr)TiO_3 thin films grown by chemical vapor deposition, J. Appl. Phys. 82 (1997) 2497–2504.

[13] R. Bouregba, G.L. Rhun, G. Poullain, G. Leclerc, Investigation of thickness dependence of the ferroelectric properties of $Pb(Zr_{0.6}Ti_{0.4})O_3$ thin-film capacitors, J. Appl. Phys. 99 (2006) 034102–7.

[14] L.-W. Chang, M. Alexe, J.F. Scott, J.M. Gregg, Settling the “dead layer” debate in nanoscale capacitors, Adv. Mater. 21 (2009) 4911–4914.

[15] Y. Gagou, J. Belhadi, B. Asbani, M. ElMarssi, J.-L. Dellis, Yu. I. Yuzyuk, I.P. Raevski, J.F. Scott, Intrinsic dead layer effects in relaxed epitaxial $BaTiO_3$ thin film grown by pulsed laser deposition, Mater. Des. 122 (2017) 157–163.

[16] B.T. Lee, C.S. Hwang, Influences of interfacial intrinsic low-dielectric layers on the dielectric properties of sputtered (Ba,Sr)TiO_3 thin films, Appl. Phys. Lett. 77 (2000) 124.

[17] H.H. Wu, J. Wang, S.G. Cao, L.Q. Chen, T.Y. Zhang, Micro-/macro-responses of a ferroelectric single crystal with domain pinning and depinning by dislocations, J. Appl. Phys. 114 (2013) 164108.

[18] Y.H. Jeon, E.A. Patterson, D.P. Cann, B.J. Gibbons, Dielectric and ferroelectric properties of $(Bi_{0.5}Na_{0.5})TiO_3$–$(Bi_{0.5}K_{0.5})TiO_3$-$BaTiO_3$ thin films deposited via chemical solution deposition, Mater. Lett. 106 (2013) 63–66.

[19] RCA clean. [Online]. Available: https://en.wikipedia.org/wiki/RCA_clean, accessed Oct. 2017.

[20] J. Suchanicz, I.P. Mercurio, P. Marchet, T.V. Kruzina, Axial pressure influence on dielectric and ferroelectric properties of $Na_{0.5}Bi_{0.5}TiO_3$ ceramic, Phys. Status. Solidi. B. 225 (2001) 459-466.

[21] W. Voigt, Lehrbuch der Kristallphysik, Leipzig, Teubner, 1910, p.369.

[22] Y. Shiratori, C. Pithan, J. Dornseiffer, R. Waser, Raman scattering studies on nanocrystalline $BaTiO_3$-Part I-isolated particles and aggregates, J. Raman Spectrosc. 38 (2007) 1288-1299.

[23] H.X. Zhang, A. Uusimaki, S. Leppavuori, P. Karjalainen, Phase-transition revealed by raman-spectroscopy in screen-printed lead-zirconate-titanate thick-films, J. Appl. Phys.76 (1994) 4294-4300.

[24] A.G.S. Filho, K.C.V. Lima, A.P. Ayala, I. Guedes, P.T.C. Freire, F.E.A. Melo, J.M. Filho, E.B. Araujo, J.A. Eiras, Raman scattering study of the $PbZr_{1-x}Ti_xO_3$ system: Rhombohedral-monoclinic-tetragonal phase transitions, Phys. Rev. B. 66 (2002) 132107-4.

[25] M. Osada, K. Nishida, S. Wada, S. Okamoto, R. Ueno, H. Funakubo, T. Katoda, Domain distributions in tetragonal Pb(Zr, Ti)O-3 thin films probed by polarized Raman spectroscopy, Appl. Phys. Lett., 87 (2005) 232902-3.

[26] H. Dong, X.J. Zheng, W. Li, Y.Q. Gong, J.F. Peng, Z. Zhu, The dielectric relaxation behavior of $(Na_{0.82}K_{0.18})_{0.5}Bi_{0.5}TiO_3$ ferroelectric thin film, J. Appl. Phys., 110 (2011) 124109-9.

[27] J.M. Rondinelli, N.A. Spaldin, Structure and properties of functional oxide thin films: insights from electronic-structure calculations, Advanced materials, 23 (2011) 3363-3381.

[28] L.J. Sinnamon, R.M. Bowman, J.M. Gregg, Investigation of dead-layer thickness in $SrRuO_3/Ba_{0.5}Sr_{0.5}TiO_3$/Au thin-film capacitors, Appl. Phys. Lett. 78 (2001) 1724-1726.

[29] J. Kreisel, A.M. Glazer, P. Bouvier, G. Lucazeau, High-pressure Raman study of a relaxor ferroelectric: The $Na_{0.5}Bi_{0.5}TiO_3$ perovskite, Phys. Rev. B. 63 (2001) 174106-10.

[30] D.Y. Wang, D.M. Lin, K.S. Wong, K.W. Kwok, J.Y. Dai, H.L.W. Chan, Piezoresponse and ferroelectric properties of lead-free $Bi_{0.5}(Na_{0.7}K_{0.2}Li_{0.1})_{0.5}TiO_3$thin films by pulsed laser deposition, Appl. Phys.Lett. 92 (2008) 222909.

[31] A.K. Tagantsev, L.E. Cross, J. Fousek, Domains in Ferroic Crystals and Thin Films, Springer Science + Bussiness Media , New York 2010 , pp. 821.

[32] Y. Bastani, T. Schmitz-Kempen, A. Roelofs, N. Bassiri-Gharb, Critical thickness for extrinsic contributions to the dielectric and piezoelectric response in lead zirconate titanate ultrathin films, J. Appl. Phys., 2011, 109 , 014115 .

[33] G. Arlt, H. Neumann, Internal bias in ferroelectric ceramics-origin and time-dependence, Ferroelectric. 87 (1988) 109-120.

[34] G.E. Pike, W.L. Warren, D. Dimos, B.A. Tuttle, R. Ramesh, J. Lee, V.G. Keramidas, J.T. Jr Evans, Voltage offsets in (Pb,La)(Zr,Ti)O-3 thin-films, Appl. Phys. Lett. 66 (1995) 484-486.

[35] D.V. Taylor and D. Damjanovic, Evidence of domain wall contribution to the dielectric permittivity in PZT thin films at sub-switching fields, J. Appl. Phys. 82(1997) 1973.